Opto-Electronic Science

ISSN 2097-0382 CN 51-1800/O4

Photo-driven fin field-effect transistors

Jintao Fu, Chongqian Leng, Rui Ma, Changbin Nie, Feiying Sun, Genglin Li and Xingzhan Wei

Citation: Fu JT, Leng CQ, Ma R, et al. Photo-driven fin field-effect transistors. *Opto-Electron Sci* **3**, 230046 (2024).

https://doi.org/10.29026/oes.2024.230046

Received: 11 December 2023; Accepted: 21 February 2024; Published online: 28 May 2024

Opto-Electronic Science

Article

May 2024, Vol. 3, No. 5

DOI: 10.29026/oes.2024.230046

Photo-driven fin field-effect transistors

Jintao Fu[1,2], Chongqian Leng[1], Rui Ma[1,3], Changbin Nie[1,2], Feiying Sun[1], Genglin Li[1,2] and Xingzhan Wei[1,2,3]*

The integration between infrared detection and modern microelectronics offers unique opportunities for compact and high-resolution infrared imaging. However, silicon, the cornerstone of modern microelectronics, can only detect light within a limited wavelength range (< 1100 nm) due to its bandgap of 1.12 eV, which restricts its utility in the infrared detection realm. Herein, a photo-driven fin field-effect transistor is presented, which breaks the spectral response constraint of conventional silicon detectors while achieving sensitive infrared detection. This device comprises a fin-shaped silicon channel for charge transport and a lead sulfide film for infrared light harvesting. The lead sulfide film wraps the silicon channel to form a "three-dimensional" infrared-sensitive gate, enabling the photovoltage generated at the lead sulfide-silicon junction to effectively modulate the channel conductance. At room temperature, this device realizes a broadband photodetection from visible (635 nm) to short-wave infrared regions (2700 nm), surpassing the working range of the regular indium gallium arsenide and germanium detectors. Furthermore, it exhibits low equivalent noise powers of 3.2×10^{-12} $W\cdot Hz^{-1/2}$ and 2.3×10^{-11} $W\cdot Hz^{-1/2}$ under 1550 nm and 2700 nm illumination, respectively. These results highlight the significant potential of photo-driven fin field-effect transistors in advancing uncooled silicon-based infrared detection.

Keywords: photodetection; silicon-on-insulator; lead sulfide; heterostructure; field-effect transistors

Fu JT, Leng CQ, Ma R et al. Photo-driven fin field-effect transistors. *Opto-Electron Sci* **3**, 230046 (2024).

Introduction

Infrared detection plays a pivotal role in modern optoelectronic systems and offers diverse applications[1–4] in fields such as spectroscopy, astronomy, night vision, and health monitoring. Traditional infrared photodetectors based on classic infrared materials[5–7] like mercury cadmium telluride (HgCdTe), indium gallium arsenide (InGaAs), and germanium (Ge) can realize excellent photodetection capability. However, these photodetectors suffer from issues like bulky module size and poor compatibility with complementary metal-oxide-semiconductor (CMOS) technology[8,9], which imposes great challenges in miniaturization and cost-effectiveness. To address these difficulties, there is a growing emphasis on merging infrared light sensing into state-of-the-art silicon (Si) electronics[1]. Unfortunately, the inherent large bandgap of Si constrains its detectable infrared light range, presenting significant obstacles to achieving this integration.

The incorporation of Si and infrared materials to create hybrid structure photodetectors stands out as the most direct solution[10–12], which effectively extends the spectral response range of Si-based devices into the infrared spectrum. These hybrid structure photodetectors mainly include photodiodes[13–15] and field-effect phototransistors[1,16–18]. Photodiodes generally suffer from low responsivity since they do not produce gain[11]. In contrast, field-effect phototransistors can achieve high gain by exploiting the photovoltage generated at the interface between infrared materials and Si to modulate device electrostatics. However, since the channel is often in a

[1]Chongqing Institute of Green and Intelligent Technology, Chinese Academy of Sciences, Chongqing 400714, China; [2]University of Chinese Academy of Sciences, Beijing 100049, China; [3]Chongqing School, University of Chinese Academy of Sciences, Chongqing 400714, China.
*Correspondence: XZ Wei, E-mail: weixingzhan@cigit.ac.cn
Received: 11 December 2023; Accepted: 21 February 2024; Published online: 28 May 2024

normally-on state, these devices tend to have a high dark current, thus degrading sensitivity. In addition, both photodiodes and field-effect phototransistors rely on planar junctions between Si and infrared materials. This planar junction constrains photogenerated charge transport and photovoltage modulation within a two-dimensional plane. As a result, the carrier transport capacity is compromised due to the restricted junction area, and modulation efficiency suffers because the photovoltage is hard to control over the entire channel. These limitations impede the performance of Si-based infrared detectors. Consequently, advancements in device architecture are required to unleash Si-based infrared detection with high sensitivity and broadband photoresponse.

In this work, a photo-driven fin field-effect transistor (photo-FinFET) is proposed to enable sensitive infrared detection. It features a fin-shaped Si strip serving as the charge transport channel, while a lead sulfide (PbS) film envelops the Si strip to function as an infrared photosensitive gate. This device structure takes inspiration from the classical microelectronic device design, the FinFET[19], which extends gate control from a two-dimensional plane to a three-dimensional space. The photo-FinFET offers two advantages: i) it leverages the PbS-Si heterojunction to better deplete the channel, maintaining it in a normally-off state and thereby reducing the dark current. ii) The photovoltage generated at the PbS-Si interface can efficiently modulate the channel, resulting in a substantial infrared photoresponse. Experimental results demonstrate that the photo-FinFET boasts a broadband photoresponse range from visible light (635 nm) to short-wave infrared (SWIR) light (2700 nm). Notably, under 1550 nm illumination, the photo-FinFET achieves a high responsivity of 45.2 A/W, a fast response speed of 150 μs, and a low equivalent noise power (NEP) of 3.2×10^{-12} W·Hz$^{-1/2}$. These outcomes underscore the potential of the photo-FinFET to merge visible and infrared photodetection on one chip while remaining compatible with the CMOS process.

Results and discussion

Device structure and working mechanism

The structural diagram of the photo-FinFET based on a PbS/Si-on-Insulator (SOI) hybrid structure is depicted in Fig. 1(a). In this configuration, the patterned Si strip positioned above the SiO_2 layer functions as the charge transport channel, while the bottom Si layer beneath the SiO_2 layer serves as the back gate. A thin PbS film is grown onto the surface of the Si channel, enveloping it and forming an infrared-photosensitive gate. Figure 1(b) illustrates the simulated energy band of the photo-FinFET, in which p-type doped PbS film (Supplementary information Section 1) forms a rectifying junction with the n-type doped Si channel. This rectifying junction induces energy band bending in the Si channel near the PbS-Si interface, thereby depleting free carriers in this region.

When exposed to infrared illumination with photon energy smaller than the Si bandgap but larger than the PbS bandgap, photogenerated carriers are exclusively created within the PbS layer (Fig. 1(c)). Subsequently, these light-excited electrons and holes separate and move in opposite directions, driven by the built-in field of the PbS-Si junction. Electrons migrate towards the Si, while holes move away into the PbS. The influx of photogenerated electrons into Si increases the concentration of free carriers in the Si channel. Moreover, the spatial separation of photogenerated electrons and holes forms a photovoltage, akin to the effect of producing an open-circuit voltage in a photodiode or solar cell[20], which compresses the depletion region and expands the conductive area in the Si channel. As a result, the electron density in the Si channel increases and its distribution is closer to the PbS-Si interface under infrared illumination compared to the dark state (Fig. 1(d–f)). In addition, the photovoltage also reduces the potential barrier in the Si channel, allowing electrons to move through the channel more efficiently (Fig. 1(g)).

The above process is equivalent to using infrared light to apply a gate voltage to turn on the transistor. Therefore, the photocurrent (I_{ph}) of the photo-FinFET can be approximately expressed as $I_{ph} \propto V_{ph} \times g_m$, where V_{ph} is the photovoltage, and g_m is the transconductance of the photo-FinFET, which is defined as $g_m = dI_{ds}/dV_{ph}$ (I_{ds} is the drain-source current). Notably, this "gate voltage modulation" induced by infrared light occurs at the PbS-Si junction surrounding the Si channel, which makes the optical gate modulation act on the Si channel in a three-dimensional manner, resulting in an obvious infrared photocurrent.

Photoelectric response characteristics

To confirm the operation mechanism of the photo-FinFET, its transfer characteristic curves were measured. As shown in Fig. 2(a) and 2(b), the transfer characteristic

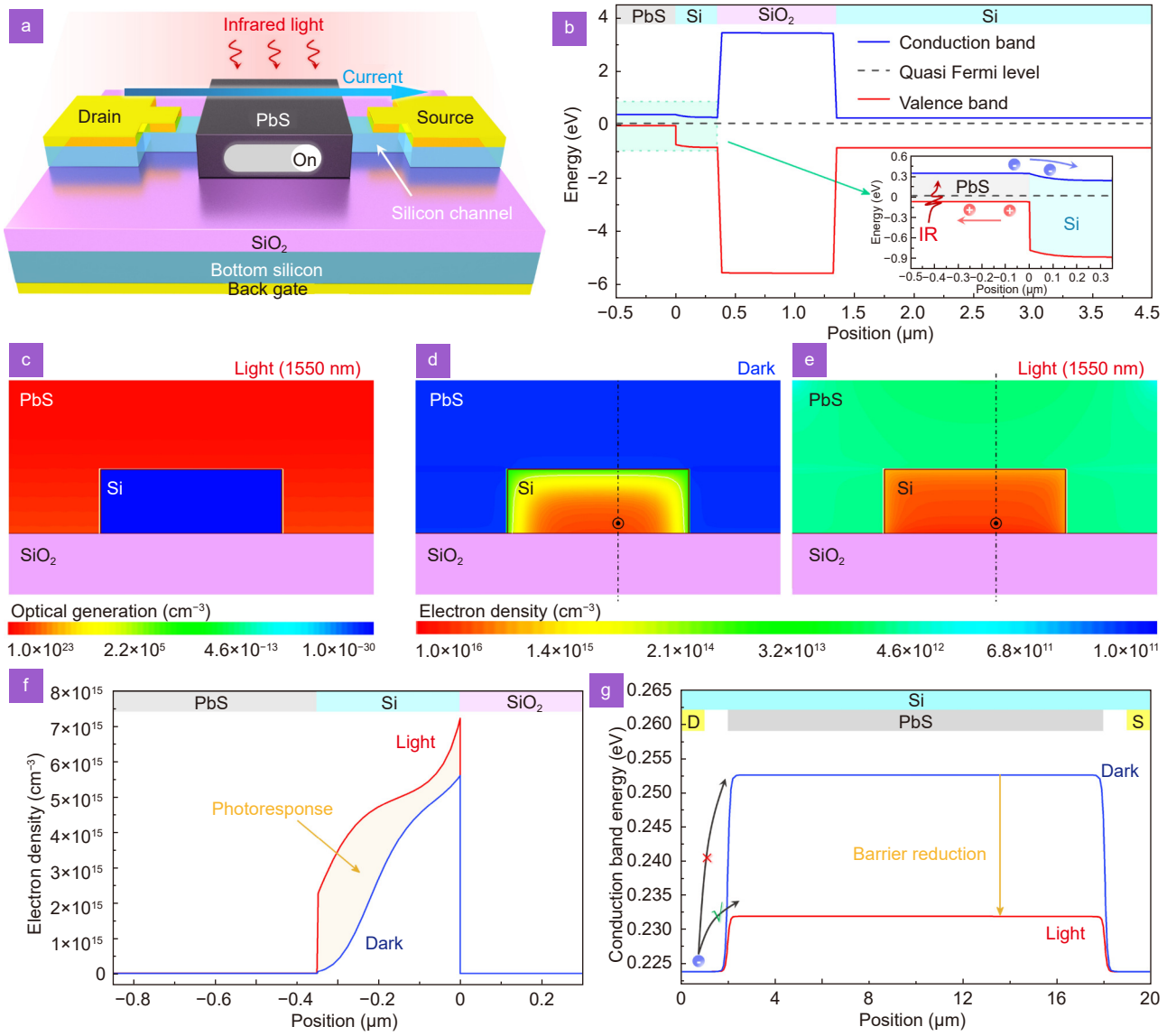

Fig. 1 | Device structure and working mechanism of the photo-FinFET. (**a**) A schematic illustration of the PbS-Si photo-FinFET. Infrared light "switches on" the PbS gate, allowing current to flow through the Si channel. (**b**) Energy band simulation results along the vertical direction of the Si channel. Inset: an enlarged view of the light green box, in which a schematic diagram of the dynamic process of photogenerated carriers under infrared illumination is depicted. (**c**) Simulated optical generation in the photo-FinFET under excitation by 1550 nm light. (**d**, **e**) Simulated electron (majority carriers) density in the photo-FinFET under darkness and 1550 nm illumination, respectively. (**f**) Electron density extracted along the dash-dotted lines in (d) and (e). (**g**) Conduction band energy extracted along the Si channel, i.e., the direction indicated by circles and dots in (d) and (e).

curve in the dark state exhibits typical n-type conduction behavior. Specifically, when a positive back gate voltage (V_{bg}) is applied, electrons accumulate in the channel, causing a rapid increase in the I_{ds} and transitioning the photo-FinFET into the "working region". In contrast, applying a negative V_{bg} leads to electron depletion in the channel, resulting in a low I_{ds} and switching the photo-FinFET into the "depletion region". Particularly, when V_{bg} is 0 V, the Si channel is depleted due to the presence of the PbS-Si junction. Therefore, I_{ds} at this point is quite low (about 7 nA). Considering that the channel of the photo-FinFET is normally off and requires a gate voltage to activate it, the photo-FinFET can be regarded as an enhancement-type transistor. This property ensures that the device maintains low energy consumption during standby[21]. When V_{bg} increases from 0 V to a positive value, the slight decrease in I_{ds} is related to the holes transferred from PbS to Si, which requires an additional positive V_{bg} to offset (Supplementary information Section 2).

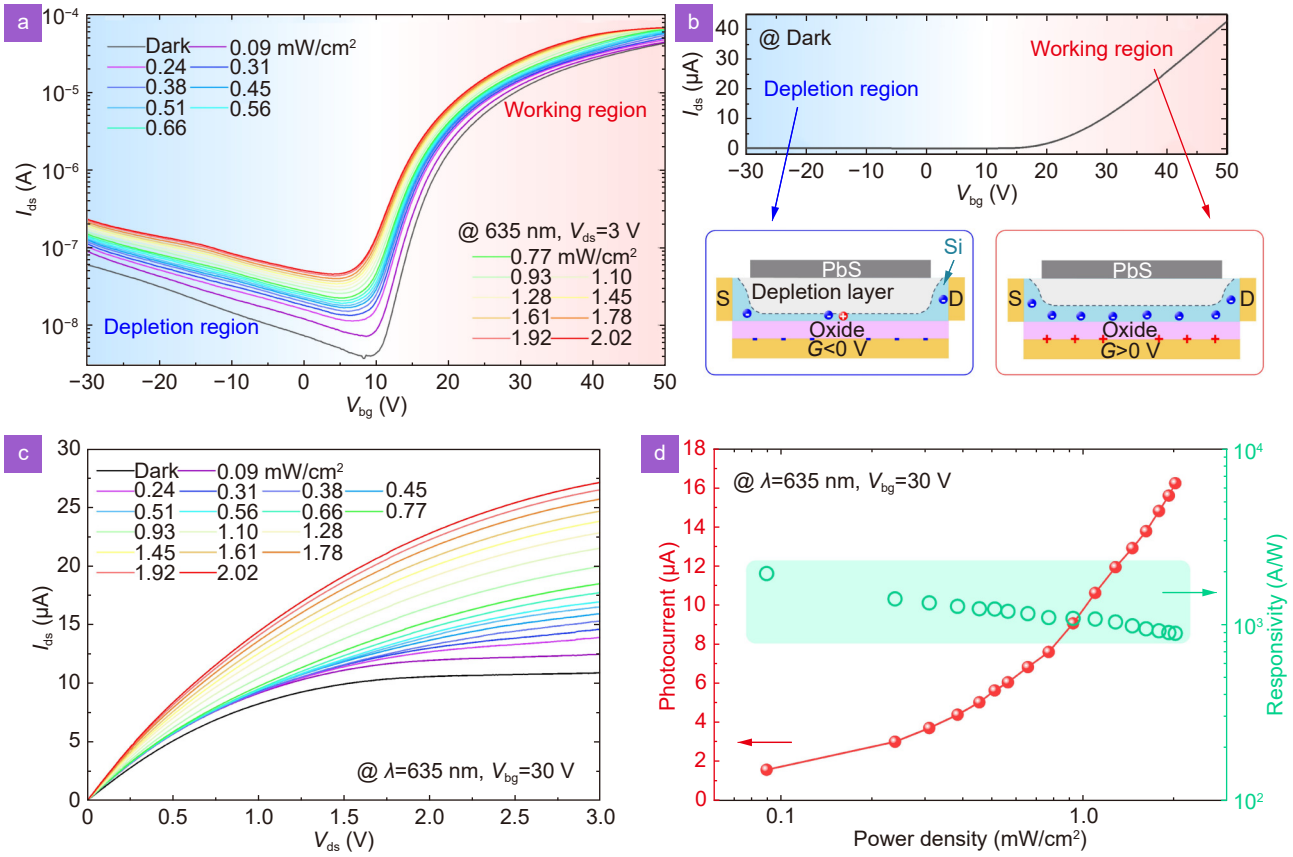

Fig. 2 | Visible photoresponse and modulation characteristic of the photo-FinFET. (**a**) Transfer characteristic curves of the photo-FinFET under 635 nm illumination with varying power densities. (**b**) Top panel: transfer characteristic curve of the photo-FinFET in the dark state. Bottom panel: schematic diagrams of the carrier dynamics process in the channel of the photo-FinFET when it is in the depletion region and working region, respectively. (**c**) Output characteristic curves of the photo-FinFET under 635 nm illumination with different power densities. (**d**) Photocurrent and responsivity as a function of light power density.

In the presence of illumination, the photo-FinFET experiences an increase in the free carriers, leading to a corresponding rise in the I_{ds}. This increase in I_{ds} is reflected in the upward shift of the transfer characteristic curve, as depicted in Fig. 2(a). As the power density of the incident light intensifies, the transfer characteristic curve demonstrates a decreasing requirement for V_{bg} to initiate a substantial increase in I_{ds}. This phenomenon can be attributed to the ability of light to compress the depletion region in the Si channel. Consequently, a relatively low V_{bg} becomes sufficient to transition the photo-FinFET from the depletion region to the working region.

Figure 2(c) displays the output characteristic curve of the photo-FinFET operating in the working region. In the dark state, as the drain-source voltage (V_{ds}) increases, I_{ds} tends to stabilize due to the occurrence of channel pinch-off —a fundamental characteristic of field-effect transistors[22]. However, upon illumination, a substantial number of photogenerated carriers are produced in the channel, making it more challenging to achieve channel pinch-off. Consequently, the phenomenon of I_{ds} stabilizing with increasing V_{ds} is less pronounced. By extracting the photocurrent, the responsivity as a function of light power density can be calculated, as illustrated in Fig. 2(d). Here, a high responsivity of 1961 A/W is observed. Details of the highest responsivity under different V_{bg} can be found in Supplementary information Section 3. The responsivity of the photo-FinFET in the working region significantly surpasses its responsivity in the depletion region. This is primarily due to the closure of the channel with V_{bg}, which substantially reduces the transconductance[22], thus weakening the photodetection capability of the photo-FinFET.

Infrared photoresponse

By configuring the photo-FinFET into the working region through V_{bg} adjustment, its infrared detection capability was evaluated. The photocurrent mapping result

of the photo-FinFET under infrared illumination (Supplementary Information Section 4) reveals that the photocurrent mainly generates within the overlapping area of the PbS-Si junction. This observation underscores the importance of the PbS-Si junction in infrared photoresponse. Figure 3(a) and 3(b) depict the *I*-*T* curves of the photo-FinFET under 1550 nm and 2700 nm illumination, respectively. It is evident that as V_{bg} increases, the photocurrent also rises, aligning with the analysis of the operation mechanism of the photo-FinFET. Under a fixed V_{bg}, the *I*-*T* curves of the photo-FinFET in response to infrared illumination with varying power densities are shown in Supplementary Information Section 5. By extracting the photocurrent and calculating the responsivity, the responsivity as a function of light power density can be obtained, as presented in Fig. 3(c) and 3(d). The highest responsivity for the photo-FinFET under 1550 nm and 2700 nm illumination is 45.2 A/W and 5 A/W, respectively. These values surpass those of traditional Si-based infrared detectors relying on cryogenic cooling equipment[23–25]. Importantly, the photo-FinFET excels at room-temperature operation, which is highly desired to enable the reduction of volume, power consumption, and cost for infrared detection systems.

Transient response and performance comparison

Next, the transient response of the photo-FinFET is characterized. Figure 4(a) displays the output signal of the photo-FinFET in response to 1550 nm illumination with a modulation frequency of 20 Hz. By amplifying the rising edge (Fig. 4(b)) and the falling edge (Fig. 4(c)) within the output signal, it is evident that the rising and falling times are 150 μs and 490 μs, respectively. The infrared response speed of the photo-FinFET closely matches its response speed in the visible spectrum (Supplementary information Section 6). Hence, under both 635 nm and 1550 nm illumination, the 3 dB bandwidth of the photo-FinFET can reach 1200 Hz (Fig. 4(d)). Moreover, by further increasing the modulation frequency of the infrared light, even up to 3000 Hz, the photo-FinFET still outputs a stable periodic signal

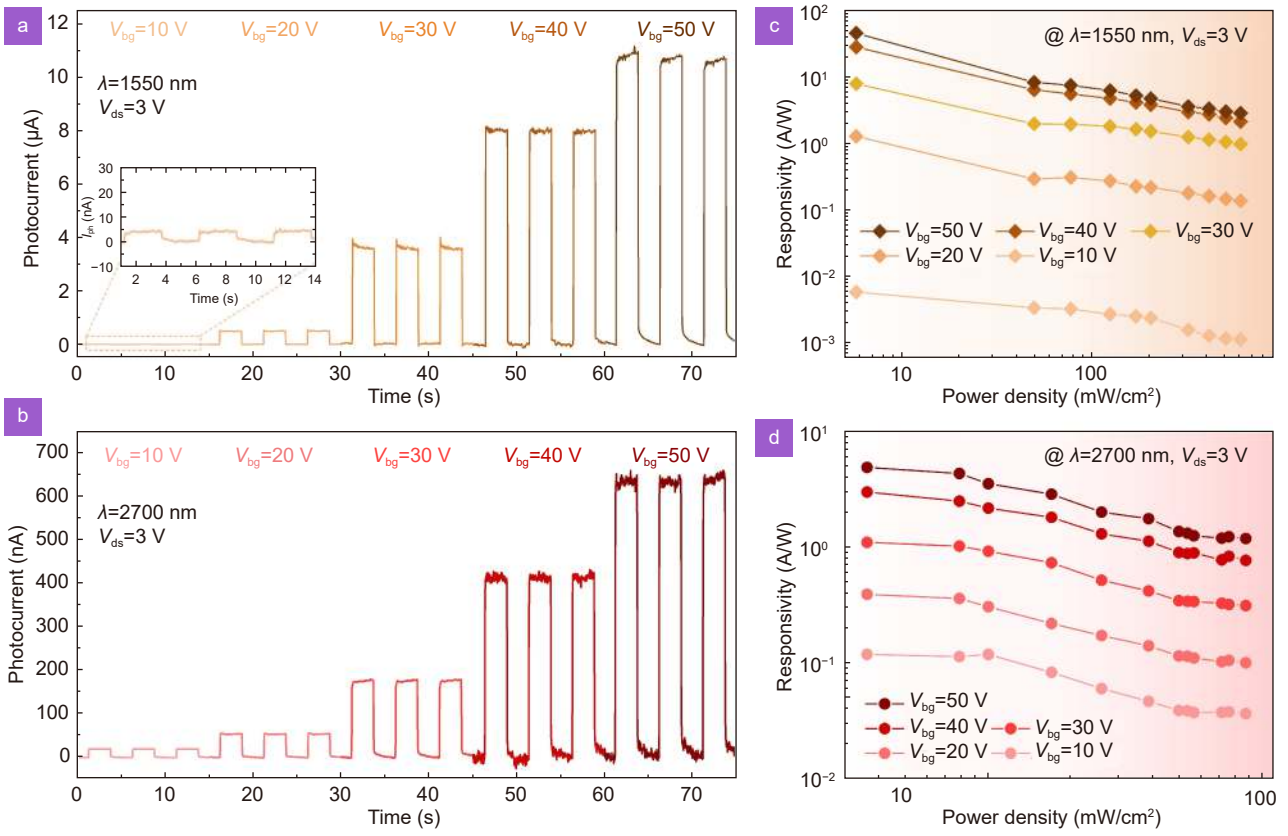

Fig. 3 | Infrared phototresponse of the photo-FinFET. (**a**, **b**) I-T curves of the photo-FinFET in response to 1550 nm and 2700 nm illumination under different V_{bg}. The power densities of the 1550 nm and 2700 nm illumination are 603.13 mW/cm² and 87.04 mW/cm², respectively. (**c**, **d**) Responsivity of the photo-FinFET as a function of the light power density under different V_{bg}. The wavelengths of the light sources are 1550 nm and 2700 nm, respectively.

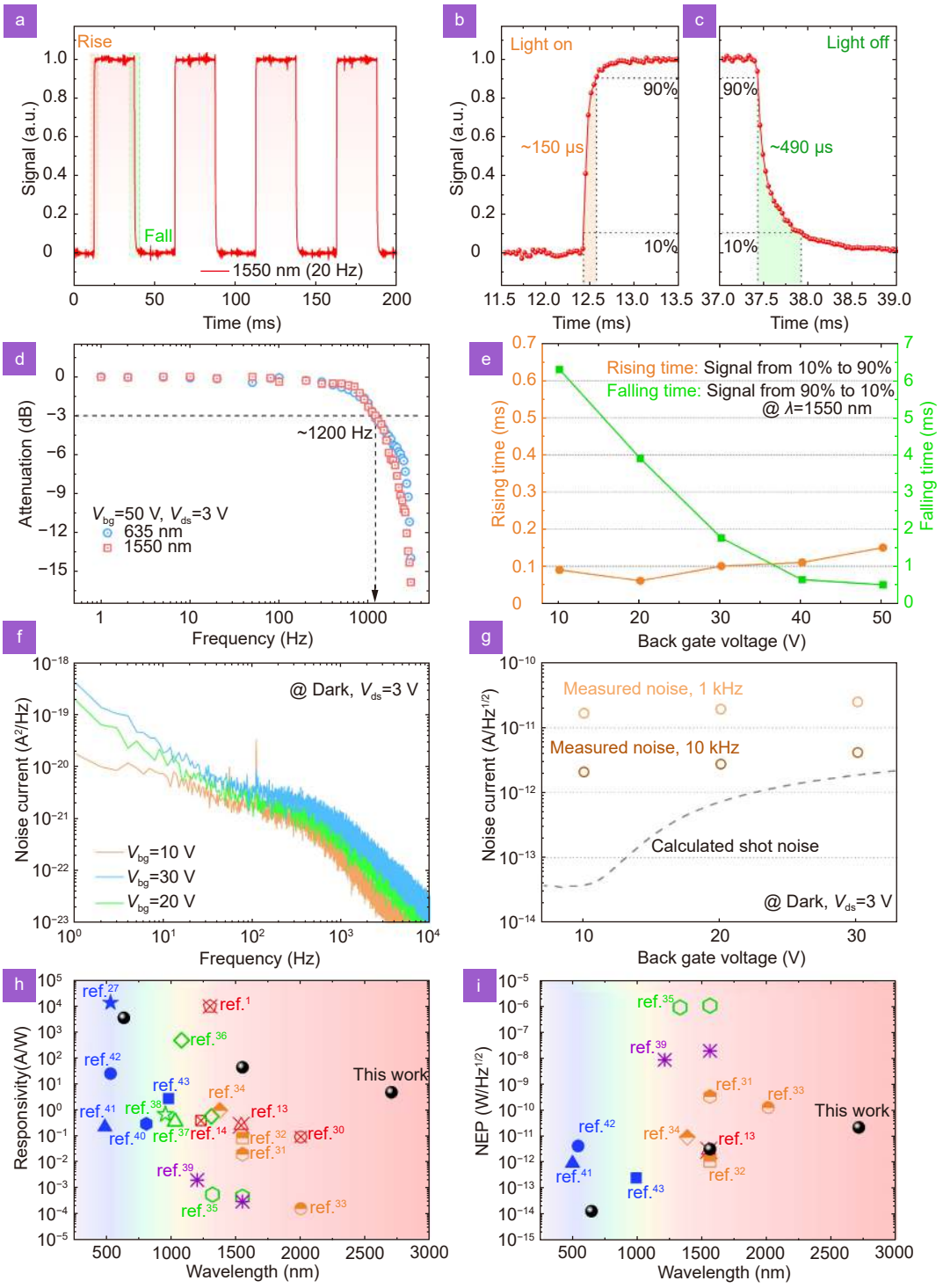

Fig. 4 | Response speed, noise and performance summary of the photo-FinFET. (**a**) Output signal of the photo-FinFET as a function of time under 1550 nm illumination. (**b**, **c**) Enlarged views of the rising and falling edges (indicated by the shaded boxed regions in (a)). (**d**) 3 dB bandwidth measurement results of the photo-FinFET under 635 nm and 1550 nm illumination. (**e**) Rising and falling times of the photo-FinFET at different V_{bg}. (**f**) Noise current of the photo-FinFET at different V_{bg}. (**g**) Measured noise current and calculated shot noise of the photo-FinFET. The calculation formula of shot noise is $2qI_{dark}$, where q is the elemental charge and I_{dark} is the dark current. (**h**, **i**) Performance comparison of the photo-FinFET with previously reported Si-based photodetectors. The responsivity and NEP of the photo-FinFET presented in (h) and (i) are measured at V_{bg} = 50 V and V_{bg} = 30 V, respectively. These previously reported Si-based photodetectors are based on different strategies to enable infrared photodetection including, integrating infrared-absorbing materials (red icons), utilizing internal photoemission effect (orange icons), manufacturing black Si (green icons), exploiting intrinsic light absorption of Si (blue icons), and hyper-doping Si (purple icons). Parameters of the photo-FinFET are indicated by black icons.

(Supplementary information Section 7). This rapid response speed meets well with the fundamental requirements of imaging equipment[26] and holds great promise for a wide range of applications. Note that the response speed of the photo-FinFET varies with V_{bg} (Fig. 4(e) and Supplementary information Section 7). An increase in V_{bg} results in a shorter falling time. This occurs because a higher gate voltage can induce a large number of additional carriers and facilitate the recombination of photogenerated carriers[27]. In contrast, the rising time is insensitive to V_{bg}. This is because the rising time is related to the infrared photoresponse process, which is affected by the separation of photogenerated carriers under the action of the built-in field in the PbS-Si junction. However, V_{bg} primarily serves to increase the electron concentration in the Si channel close to the SiO_2 side and has a negligible impact on the state of the PbS-Si junction (Supplementary information Section 8).

Furthermore, the noise currents of the photo-FinFET under various V_{bg} were measured, and the corresponding results are presented in Fig. 4(f). In the low-frequency range, the dominant noise source is $1/f$ noise[28]. As the frequency increases, the observed bump in noise current can be attributed to random telegraph noise introduced by the external bias voltage[29]. In the high-frequency range, noise current decreases with increasing frequency, consistent with the behavior observed in previous Si-based phototransistors[1]. By extracting the noise currents at 1 kHz and 10 kHz (Fig. 4(g)), it can be observed that as V_{bg} increases, the noise current also rises. The reason for the increase in noise is that a higher gate voltage induces a greater number of free charges within the Si channel, thereby increasing the probability of random carrier fluctuations. Nevertheless, the noise currents of the photo-FinFET remain low. This outcome benefits from the high-quality interface between the Si channel and the SiO_2 layer, as well as the depletion effect of the PbS-Si junction, both of which enable efficient carrier transport within the Si channel rather than being scattered by surface states. Based on the measured noise current, the NEP of the photo-FinFET under 1550 nm illumination can be calculated to be 3.2×10^{-12} W·Hz$^{-1/2}$ (at V_{bg} = 30 V, 1 kHz). Similarly, the NEP of the photo-FinFET in response to 2700 nm illumination can be obtained as 2.3×10^{-11} W·Hz$^{-1/2}$.

To assess the performance of the photo-FinFET, it has been compared with previously reported Si-based photodetectors. These Si-based photodetectors[1,13,14,27,30–43] employ various specialized techniques to achieve infrared photodetection (Supplementary Information Section 9). As depicted in Fig. 4(h), the photo-FinFET not only exhibits a responsivity on par with these devices in the visible and near-infrared spectral range but also demonstrates impressive capabilities in SWIR detection. Furthermore, owing to the low noise characteristics, the NEP of the photo-FinFET even surpasses that of the majority of these devices (Fig. 4(i)).

Conclusions

In conclusion, a photo-FinFET that is capable of sensitive SWIR detection has been designed and fabricated. At room temperature, the photo-FinFET demonstrates low NEPs of 3.2×10^{-12} W·Hz$^{-1/2}$ and 2.3×10^{-11} W·Hz$^{-1/2}$ under 1550 nm and 2700 nm illumination, respectively. Moreover, the photo-FinFET offers the advantage of gate voltage-tunable photodetection performance, including responsivity, response speed, and NEP, thus enhancing flexibility when selecting suitable application conditions. The intriguing architecture of the photo-FinFET creates a three-dimensional infrared-activated gate, efficiently leveraging the photovoltage to drive the field-effect transistors.

Method

PbS thin film synthesis

The PbS film was synthesized by the chemical bath deposition (CBD) method. Lead acetate ($Pb(CH_3COO)_2$) (3.225 g), sodium hydroxide (NaOH) (1.14 g), thiourea (NH_2CSNH_2) (0.57 g), and tri-sodium citrate ($C_6H_5Na_3O_7$) (2.205 g) were dissolved in 25 mL deionized water, respectively. The solution is mixed in the order of lead acetate solution, sodium hydroxide solution, thiourea solution, and trisodium citrate solution. The fixture with samples was placed in the mixed solution. Subsequently, the beaker was put in a chemical water bath pot to grow the PbS film at 40 °C water bath for 1 hour. After the reaction was completed, the beaker was placed in the water of the ultrasonic cleaning machine for 5 seconds to remove the clusters deposited on the surface of PbS films. The samples were then cleaned with deionized water and dried with N_2. The characterization results about the thickness and morphology of the PbS film can be seen in Supplemental information Section 10.

Device fabrication

A SOI substrate was used to fabricate the photo-FinFET. First, the Si channels were defined by lithography and patterned by dry etching. Using the Si channel as a reference, aligning lithography was exploited to define the drain and source electrodes. Subsequently, Cr (5 nm)/Au (50 nm) was deposited by magnetron sputtering, followed by a lift-off process. The entire backside of the SOI substrate was sputtered with Au (50 nm) as the back gate electrode. The PbS pattern was defined by a second aligning lithography, using the electrode as a reference. Next, the PbS film was grown on the SOI substrate by the CBD method. Finally, the excess PbS was removed through a lift-off process in acetone to obtain photo-FinFETs. The PbS film does not make direct contact with the source and drain electrodes, ensuring electrical isolation from each other. The corresponding schematic diagram of the fabrication process and parameters of the SOI substrate can be found in Supplementary information Section 11.

Device simulation

The energy band, electron density profile, conduction band energy, and electrostatic potential in the photo-FinFET were simulated by technology computer-aided design software. The physical models used during the simulation include Fermi-Dirac statistics, Poisson distribution, continuity formulation, drift-diffusion equation, doping-related recombination, and optical excitation. The doping concentrations of PbS, top Si layer, and bottom Si layer were assumed to be 3×10^{13} cm^{-3}, 5×10^{15} cm^{-3}, and 5×10^{15} cm^{-3}, respectively. The contact between the electrode and the material was set as Ohmic contact.

Photoelectric response measurement

The electrical characteristics of the photo-FinFET were measured by a Keithley 4200-scs semiconductor analyzer. The light sources used in the experiment included 635 nm, 1550 nm, and 2700 nm lasers, and their power was calibrated with a commercial optical power meter (Thorlabs S405C). The photocurrent mapping was obtained by scanning over the photo-FinFET using a scanning Galvo System (Thorlabs GVS212) with a focused 1550 nm laser beam (Spot diameter is ~2 μm). To evaluate the response speed, an oscilloscope (Tektronix DPO 5204) was used to collect the output signal of the photo-FinFET. The periodic switching of the light source was realized by connecting the laser with a signal generator (RIGOL DG1022U). The noise spectrum analyzer used for noise current measurement was provided by Shenzhen Liangwei Co., Ltd. The maximum voltage that the noise spectrum analyzer can apply is 30 V.

References

1. Adinolfi V, Sargent EH. Photovoltage field-effect transistors. *Nature* **542**, 324–327 (2017).
2. Yan HL, Li HN, Wang S et al. Overview of the LAMOST survey in the first decade. *Innovation* **3**, 100224 (2022).
3. Li CH, Du W, Huang YX et al. Photonic synapses with ultralow energy consumption for artificial visual perception and brain storage. *Opto-Electron Adv* **5**, 210069 (2022).
4. Zhang WL, Çakıroğlu O, Al-Enizi A et al. Solvent-free fabrication of broadband WS_2 photodetectors on paper. *Opto-Electron Adv* **6**, 220101 (2023).
5. Rogalski A. *Infrared Detectors* (CRC Press, Location, 2000).
6. Hu WD, Chen XS, Ye ZH et al. A hybrid surface passivation on HgCdTe long wave infrared detector with *in-situ* CdTe deposition and high-density hydrogen plasma modification. *Appl Phys Lett* **99**, 091101 (2011).
7. Hu WD, Ye ZH, Liao L et al. 128 × 128 long-wavelength/mid-wavelength two-color HgCdTe infrared focal plane array detector with ultralow spectral cross talk. *Opt Lett* **39**, 5184–5187 (2014).
8. Zeng LH, Han W, Ren XY et al. Uncooled mid-infrared sensing enabled by chip-integrated low-temperature-grown 2D $PdTe_2$ dirac semimetal. *Nano Lett* **23**, 8241–8248 (2023).
9. Rogalski A. Infrared detectors: status and trends. *Prog Quantum Electron* **27**, 59–210 (2003).
10. Wu PS, Ye L, Tong L et al. Van der Waals two-color infrared photodetector. *Light Sci Appl* **11**, 6 (2022).
11. Zhou W, Zheng L, Ning ZJ et al. Silicon: quantum dot photovoltage triodes. *Nat Commun* **12**, 6696 (2021).
12. Yan SQ, Zuo Y, Xiao SS et al. Graphene photodetector employing double slot structure with enhanced responsivity and large bandwidth. *Opto-Electron Adv* **5**, 210159 (2022).
13. Xu KM, Xiao XB, Zhou WJ et al. Inverted Si: PbS colloidal quantum dot heterojunction-based infrared photodetector. *ACS Appl Mater Interfaces* **12**, 15414–15421 (2020).
14. Masala S, Adinolfi V, Sun JP et al. The silicon: colloidal quantum dot heterojunction. *Adv Mater* **27**, 7445–7450 (2015).
15. Michel J, Liu JF, Kimerling LC. High-performance Ge-on-Si photodetectors. *Nat Photonics* **4**, 527–534 (2010).
16. Shi YL, Wu ZM, Xiang ZH et al. Silicon-based PbS-CQDs infrared photodetector with high sensitivity and fast response. *Nanotechnology* **31**, 485206 (2020).
17. Shi YL, Wu ZM, Dong X et al. A silicon-based PbSe quantum dot near-infrared photodetector with spectral selectivity. *Nanoscale* **13**, 12306–12313 (2021).
18. Chen PY, Wu ZM, Shi YL et al. High-performance silicon-based PbSe-CQDs infrared photodetector. *J Mater Sci Mater Electron* **32**, 9452–9462 (2021).
19. Ferain I, Colinge CA, Colinge JP. Multigate transistors as the future of classical metal–oxide–semiconductor field-effect transistors. *Nature* **479**, 310–316 (2011).
20. Li MH, Zhou JJ, Tan LG et al. Multifunctional succinate additive for flexible perovskite solar cells with more than 23% power-

conversion efficiency. *Innovation* **3**, 100310 (2022).
21. Parmar JS, Sahu C. CMOS-compatible ex-situ incorporated junctionless enhancement-mode thin polysilicon film FET pH sensor. *IEEE Trans Device Mater Reliab* **21**, 2–8 (2021).
22. Sze SM, Ng KK. *Physics of Semiconductor Devices* 3rd ed (Wiley-Interscience, Hoboken, 2007).
23. Belin AM, Zolotarev VI, Nikiforov AY et al. 320 × 240 CMOS array for the spectral range of 3–5 μm based on PtSi photodiodes. *Russ Microelectron* **45**, 474–477 (2016).
24. Wu JH, Chang RS, Horng GJ. Microstructure, electrical, and optical properties of evaporated PtSi/p-Si(100) Schottky barriers as high quantum efficient infrared detectors. *Thin Solid Films* **466**, 314–319 (2004).
25. Kay R, Bean R, Zanio K et al. HgCdTe photovoltaic detectors on Si substrates. *Appl Phys Lett* **51**, 2211–2212 (1987).
26. Liu J, Liu PL, Chen DY et al. A near-infrared colloidal quantum dot imager with monolithically integrated readout circuitry. *Nat Electron* **5**, 443–451 (2022).
27. Fu JT, Nie CB, Sun FY et al. Photo-driven semimetal–semiconductor field-effect transistors. *Adv Opt Mater* **11**, 2201983 (2023).
28. Vandamme EP, Vandamme LKJ. Critical discussion on unified 1/f noise models for MOSFETs. *IEEE Trans Electron Devices* **47**, 2146–2152 (2000).
29. Almeida JM, Wisniowski P, Freitas PP. Low-frequency noise in MgO magnetic tunnel junctions: Hooge's parameter dependence on bias voltage. *IEEE Trans Magn* **44**, 2569–2572 (2008).
30. Cong H, Xue CL, Zheng J et al. Silicon based GeSn p-i-n photodetector for SWIR detection. *IEEE Photonics J* **8**, 6804706 (2016).
31. Casalino M, Sassi U, Goykhman I et al. Vertically illuminated, resonant cavity enhanced, graphene-silicon schottky photodetectors. *ACS Nano* **11**, 10955–10963 (2017).
32. Goykhman I, Sassi U, Desiatov B et al. On-chip integrated, silicon-graphene plasmonic schottky photodetector with high responsivity and avalanche photogain. *Nano Lett* **16**, 3005–3013 (2016).
33. Casalino M, Russo R, Russo C et al. Free-space schottky graphene/silicon photodetectors operating at 2 μm. *ACS Photonics* **5**, 4577–4585 (2018).
34. Tanzid M, Ahmadivand A, Zhang RM et al. Combining plasmonic hot carrier generation with free carrier absorption for high-performance near-infrared silicon-based photodetection. *ACS Photonics* **5**, 3472–3477 (2018).
35. Hu F, Dai XY, Zhou ZQ et al. Black silicon Schottky photodetector in sub-bandgap near-infrared regime. *Opt Express* **27**, 3161–3168 (2019).
36. Huang S, Wu Q, Jia ZX et al. Black silicon photodetector with excellent comprehensive properties by rapid thermal annealing and hydrogenated surface passivation. *Adv Opt Mater* **8**, 1901808 (2020).
37. Zhao XN, Lin K, Zhao B et al. Broadband MSM photodetector based on S-doped black silicon fabricated by femtosecond laser. *Appl Surf Sci* **619**, 156624 (2023).
38. Zhang YB, Loh JYY, Kherani NP. Facilely achieved self-biased black silicon heterojunction photodiode with broadband quantum efficiency approaching 100%. *Adv Sci (Weinh)* **9**, 2203234 (2022).
39. Wang M, García-Hemme E, Berencén Y et al. Silicon-based intermediate-band infrared photodetector realized by Te hyperdoping. *Adv Opt Mater* **9**, 2001546 (2021).
40. Wang L, Jie JS, Shao ZB et al. MoS_2/Si heterojunction with vertically standing layered structure for ultrafast, high-detectivity, self-driven visible-near infrared photodetectors. *Adv Funct Mater* **25**, 2910–2919 (2015).
41. An XH, Liu FZ, Jung YJ et al. Tunable graphene-silicon heterojunctions for ultrasensitive photodetection. *Nano Lett* **13**, 909–916 (2013).
42. Huang K, Yan YC, Li K et al. High and fast response of a graphene-silicon photodetector coupled with 2D fractal platinum nanoparticles. *Adv Opt Mater* **6**, 1700793 (2018).
43. You S, Zhang L, Yu YQ et al. Nanoscale $AgInTe_2$/Si truncated quasitetrahedrons for heterostructured photodetectors. *ACS Appl Nano Mater* **4**, 5785–5795 (2021).

Acknowledgements

This work was supported by the National Key R&D Program of China (2017YFE0131900), the Natural Science Foundation of Chongqing, China (CSTB2023NSCQ-LZX0087), and the National Natural Science Foundation of China (62204242, 62005182).

Author contributions

JT Fu and XZ Wei conceived the idea. JT Fu carried out the experiments including device fabrication, device simulation and performance characterization with the help of CQ Leng, GL Li, CB Nie, and FY Sun. CQ Leng made the growth of PbS. R Ma made the characterization of PbS. JT Fu and XZ Wei made the analytical analysis. JT Fu and XZ Wei wrote the manuscript with comments from all the other authors. XZ Wei supervised the project.

Competing interests

The authors declare no competing financial interests.

Supplementary information

Supplementary information for this paper is available at https://doi.org/10.29026/oes.2024.230046

Scan for Article PDF